This document is confidential and is proprietary to the American Chemical Society and its authors. Do not copy or disclose without written permission. If you have received this item in error, notify the sender and delete all copies.

Life Aging Effect as a Conditioning Process that Regulates the Performance of the Halogen-Free Mg Electrolyte

Journal:	*Langmuir*
Manuscript ID	Draft
Manuscript Type:	Article
Date Submitted by the Author:	n/a
Complete List of Authors:	Sheha, Eslam; Benha University, Physics Fan, Shengqi; University of Massachusetts Boston Farrag, Mohamed; Benha University, Physics El-Dok, Engy ; Benha University Faculty of Science Sulatt, Dora ; UMASS Sa, Niya; University of Massachusetts Boston College of Science and Mathematics, Chemistry

SCHOLARONE™
Manuscripts

Life Aging Effect as a Conditioning Process that Regulates the Performance of the Halogen-Free Mg Electrolyte

Eslam Sheha*[1], Shengqi Fan[2], Mohamed Farrag[1], Engy El-Dok[3], Dora Sulatt[2], Niya Sa*[2]

[1]Physics Department, Faculty of Science, Benha University,13518, Benha, Egypt

[2]Department of Chemistry, University of Massachusetts Boston, Boston, Massachusetts 02125, United States of America

[3]Chemistry Department, Faculty of Science, Benha University,13518, Benha, Egypt

niya.sa@umb.edu & islam.shihah@fsc.bu.edu.eg

Abstract

Studying the interplay of the electrochemical performance and the electrolyte conditioning process is crucial for building an efficient magnesium battery. In this work, we use halogen-free electrolyte (HFE) based on $Mg(NO_3)_2$ in acetonitrile (ACN) and tetraethylene glycol dimethyl ether (G4) to study the effect of the aging time calendar on its electrochemical properties. The characterization techniques confirm apparent changes occurring in the bulk speciation and the Mg^{2+} solvation barrier of the aging HFE relative to the as-prepared fresh HFE. The overpotential of Mg plating/stripping and bulk resistance of aging HFE is reduced relative to the as-prepared fresh HFE. Mg-S cells using aged HFE deliver high specific capacities (586 mAh/g), higher Coulombic efficiencies, and higher cycle life (up to 30 cycles at 25 °C) relative to Mg-S cells with fresh HFE that deliver a specific capacity of ~ 535 mAh g^{-1}, low coulombic efficiency, and short cycle life; at a current density of 0.02 mA cm^{-2}. The present findings provide a new concept describing how the aging process regulates the electrochemical performance of HFE and enhance the cycle life of Mg-S batteries.

Keywords: Magnesium-ion battery; Halogen-free electrolyte; The aging process; Conditional mechanisms

Introduction

Rechargeable magnesium batteries (RMBs) are nominated to be one of the most promising next-generation "beyond Li-ion" because of the merits of using Mg anodes, which offers a low reduction potential (-2.36 V vs. NHE), low dendritic growth, low air sensitivity, high volumetric capacity ~3833 mAh cm^{-3} (twice of the Li metal), sustainability, safety, and low cost[1]. Unfortunately, the high charge density for Mg^{2+} ion (120 $C.mm^{-3}$) generates a strong electrostatic interaction with its surrounding, resulting in sluggish Mg^{2+} ion diffusion kinetic in most materials and high reactivity of Mg metal toward electrolyte species[2]. Magnesium-sulfur (Mg-S) battery chemistry bypasses the intercalation issues via adapting conversion reaction results in superior theoretical specific capacity (1673 mAh g^{-1})[3]. However, the electrophilic nature of the sulfur element requested the development of a new series of non-nucleophilic electrolytes such as magnesium tetrakis(hexafluoroisopropyloxy) borate to alleviate electrolyte decomposition and overcome the short cycle life time[3, 4]. However, open questions are still causing short cycle life, such as high cost, complicated synthesis process, low oxidation potential, and the conditioning process[5]. Hence, much work must be devoted to designing, synthesizing, and optimizing novel Mg electrolytes to realize the practical application of Mg batteries. Recent progress in this area touches on tailoring the interfacial charge transfer kinetics using chelants agents[6], weakly coordinating solvent (tetrahydrofuran, THF)[7], and corrosion inhibitor additives[8]. Magnesium electrolytes require electrolytic conditioning to exhibit reversible Mg electrodeposition and low overpotential[9]. Galvanostatic cycling is one of the significant conditioning processes that helps scavenge the active contaminants from the electrolyte solution[10 11]. There are scarce research about the aging time strategy on tailoring the radius of solvation shells or the interfacial charge transfer kinetics of the non-nucleophilic electrolytes. In this work, we knock on a new door of the aging time strategy

as a new conditioning process that regulates the electrochemical performance of the magnesium electrolytes. In our previous research,[4] we reported simple halogen-free electrolyte HFE (0.69 M $Mg(NO_3)_2 \cdot 6H_2O$ in ACN:G4(~2:1) with a promising utilization in Mg/S battery, in this report, the role of aging time as a new strategy in understanding the electrochemical performance of the HFE is investigated. Furthermore, aiming to reduce the shuttle effect of soluble intermediate species (polysulfide), $BaTiO_3$ as piezoelectric materials is a multifunctional additive generats electrostatic charges on the surfce due to the electrochemical stress. The surface charges trap the polar polysulfide molecules and reduce the rate of polysulfide shuttling so does improve the cycle life of Mg-S cells.[12, 13] Attenuated total reflection Fourier transform infrared (ATR-FTIR) spectrscopy, UV-Vis spectrscopy, electrochemical impedance spectrscopy EIS, cyclic voltametry and the glvanostatic cycling were conducted to track the evolution of the electrochemical performance for the HFE with aging time. Fundamental insights into the Mg interface of Mg(Mg half cells) and the formed film's nature were conducted using FTIR, X-ray diffraction (XRD) and SEM techniques. Furthermore, Mg-S cell with fresh and aging HFE were assempeled and tested for potential applications. A systematic investigation into the morphology and the structure of the S cathodes in aging HFE at different electrochemical states was conducted using SEM, EDX, XRD and EIS. By integrating these characterization techniques, we confirm the impact of aging calendar as conditioning process that regulates the electrochemical performance of the halogen-free Mg electrolyte via modulating the radius of solvation shells and the ion-diffusion.

Experimental Technique

HFE-based magnesium nitrate hexahydrate was prepared according to our previous research[4]. The electrolyte was left in the dark at different aging times. Cyclic voltammograms (CV) were recorded in an electrochemical cell constructed with a Pt disk as the working electrode (2.0 mm in diameter),

and polished Mg foil (99.9% purity, Sigma-Aldrich) as the reference electrode and the counter electrode. The electrochemical measurements were conducted within an argon-filled glovebox (Vacuum Technology Inc.) with H_2O and O_2 levels under 1.0 ppm. Mg deposition was obtained in the > 1 month HFE electrolyte using chronopotentiometry at –2 V for 12 h. The obtained Mg deposit was rinsed with DMC and dried under vacuum for 2 h before imaging. Microstructure characterization was carried out via scanning electron microscopy (Sigma500VP FESEM, Zeiss) and the elemental mappings were performed by an energy-dispersive spectrometer (EDS, Oxford Instruments). A galvanostatic test was performed on a NEWARE BTS4000 at a current density of 20 μAh cm^{-2} at 25 °C. UV-Vis was conducted using Edinburgh DS5 Dual Beam UV-Vis spectrophotometer. ATR-FTIR spectroscopy was conducted using Bruker Alpha II spectrophotometer. The protocol of cathode synthesis is as follows: 75 wt.% Sulfur (S, Alfa Aesar 99%), 5 wt.% $BaTiO_3$ (Alfa Aesar 99%) and 20 wt.% Graphene was ground, and the sulfur was exfoliated and evaporated at the surface of the GNP flakes and BTO via 10 seconds a pulse of 1200 Watt microwave oven. N-methyl-2- pyrrolidinone solution was added to the mixture of 75 wt. % active material, 10 wt. % Super P, and 15 wt. % PVDF to form a viscous slurry, then pasted on the current collector of Al foil using a mini-coater (MC-20, Hohsen) with a thickness of approximately 100 μm. Afterward, the film was dried in an oven at 100 °C for two h, and the active sulfur mass loadings were within 0.45 mg cm^{-2}. XRD pattern was recorded for the collected electrodes from the half and full cells using the Rigaku MiniFlex 600 diffractometer with Cu Kα-radiation. Scanning electron microscope (SEM) images were recorded using Jeol JMS-700 equipped with energy-dispersive. Electrochemical impedance spectroscopy EIS of half and full cells, cyclic voltammetry of Mg|Electrolyte|S cells, linear seep voltammetry of

Results and discussion

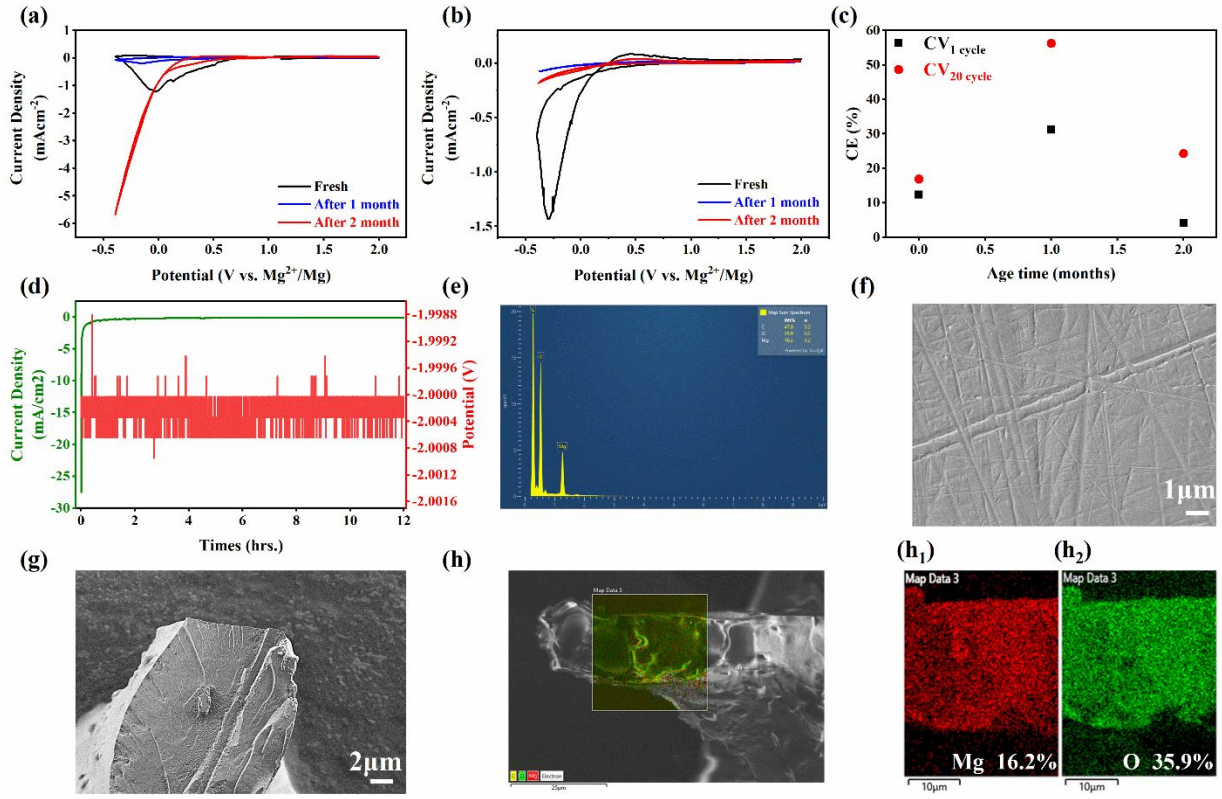

Fig. 1 CVs on the platinum working electrode of fresh and aging HFE at a scan rate of 50mV/s; (a) First cycle (b) After 20 cycles; (c) Coulombic efficiency vs. Age time; (d) Chronoamperometry and Potential curve; (e) EDS spectrum for the electrochemically plated Mg in the > 1 month electrolyte; (f-h) SEM and EDS elemental mapping images of plated Mg metal in the > 1 month electrolyte.

Mg|Electrolyte|Stainless-steel cells were recorded using an electrochemical workstation model CHI605E. To investigate the impact of aging time on the electrochemical characteristics of halogen-free electrolyte HFE (0.69 M $Mg(NO_3)_2 \cdot 6H_2O$ in ACN:G4(~2:1)), the 1st and 20th CV cycles of an aging HFE were examined and compared to a freshly prepared HFE as shown in Fig.1 (a-b), respectively. A significant increase in cathodic peak current density was observed in the aged HFE after 2 months during the first CV cycle, likely attributed to a lower de-solvation energy

barrier caused by a change in the solvation structure of Mg center upon aging. The coulombic efficiency of freshly prepared and aging HFE is presented in Fig.1(c). The higher coulombic efficiency values after 20 CV cycles than those of the first CV cycle could be ascribed to the formation and growth of solid electrolyte layer at electrode surface. **Fig.1(d)** depicts the chronoamperometry (CA) profile acquired on the Pt electrode under the applied potential of -2 V for a duration of 12 hours in aging HFE. The white solid powder of Mg deposition was obtained on the Pt electrode surface, as further evidenced by the SEM image and EDS results displayed in Fig.1(e) and Fig.1(g-f), respectively. In **Fig.1(h)**, the EDS elements mapping images of Mg deposition gained in aging HFE exhibit a uniform distribution of Mg and O elements. The relatively higher percentage of O (35.9% wt.%) compared to Mg (16.2 wt.%) might potentially arise from the abundant decomposition in aging HFE. ATR-FTIR spectroscopy is a powerful technique used to test the functional group's evolution of the targeted materials. **Fig. 2(a-c)** shows the ATR-FTIR spectra of the as-prepared fresh and aging electrolyte in the range of 400-4000 cm^{-1}. The spectra are consistent with a series of peaks matching the previous FTIR study of HFE[14]. In Fig.2b, three changes in FTIR features were observed in the aged HFE electrolyte as compared to the freshly prepared HFE. The signature of the -C≡N stretching at 2256 cm^{-1} is shifted to 2252 cm^{-1} upon aging, indicating reduced vibration of CH_3CN due to the coordination with Mg ions or hydrogen[15]. The emergence of the peaks at 2293 cm^{-1} and 2360 cm^{-1} in aging HFE are potentially assigned to the vibration of -C ≡ N−H-O(H)---Mg^{2+} and -C ≡ N---Mg^{2+}, respectively[16]. This finding suggests the association of the H_2O and ACN molecules with the Mg center with storage. The intensity of characteristic peaks of the fresh HFE increases with life aging; however, aging over a month reduces the intensity of some peaks, like the C≡N stretch of ACN[17]. UV–Visible absorption results electronic transition of the absorbing species, so does UV–Visible spectroscopy.

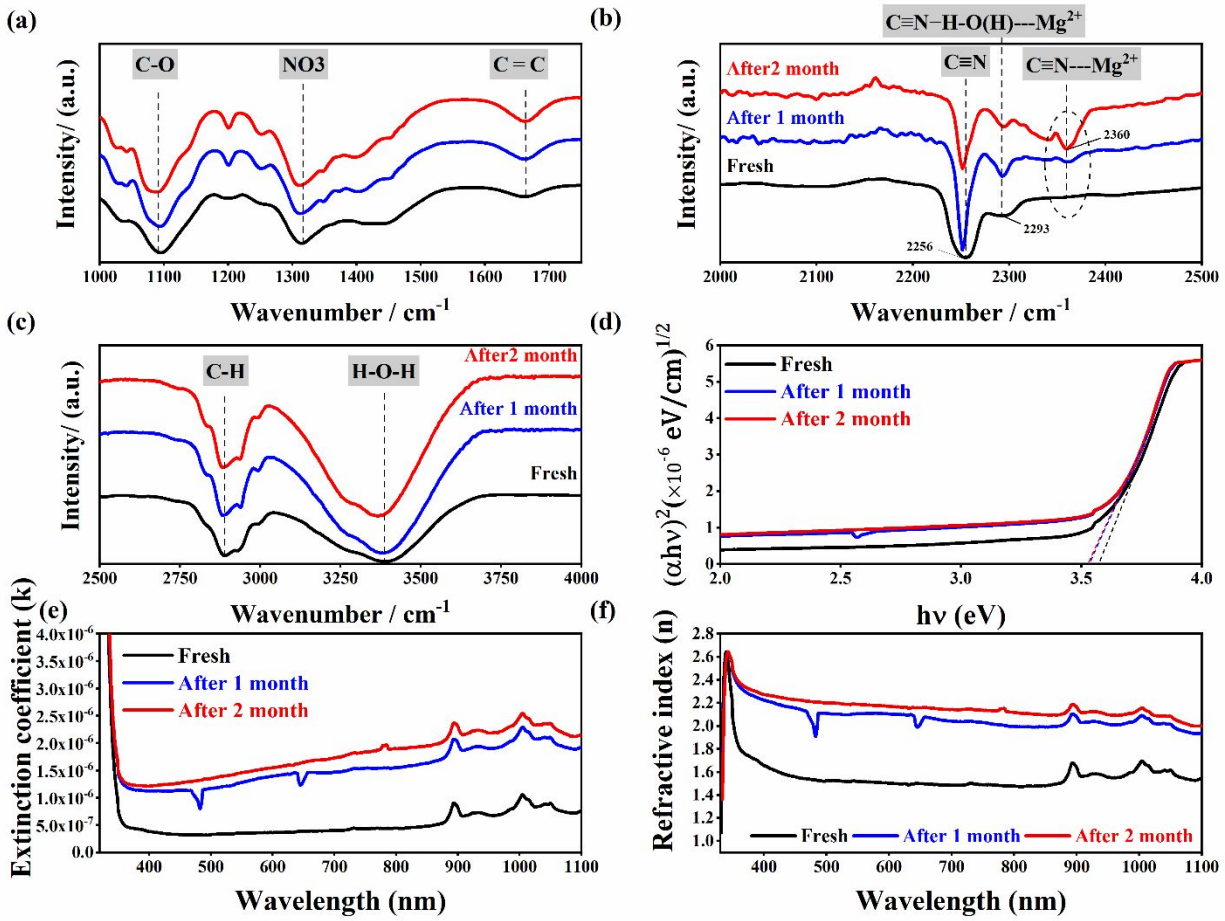

Fig. 2 (a-c) ATR-FTIR spectra (d) Tauc's plot (e)Extinction coefficient (f); Refractive index; for fresh and aging HFE.

offers a useful method to examine quantitatively diverse analytes such as transition metal ions, biological macromolecules and conjugated organic molecules. **Fig. 2(d-f)** shows the UV–Visible absorption spectrum of fresh and aging HFE in the range of 200-1100 nm. Conventional Tauc's relation: $\alpha h\nu = \beta[h\upsilon - E_g]^n$ is used to calculate accurate bandgap values from UV–Visible spectra, where $\alpha = 2.303\frac{A}{t}$, A, hυ, β, and n are the absorption coefficient, absorbance, incident photon energy, fitting constant, and an exponent = 1/2 or 2 for direct/indirect transition from the valence band to the conduction band, respectively. **Fig. 2 d** displays the direct electronic transition plot of hν versus $(\alpha h\nu)^{0.5}$ for fresh and aging HFE. It is worth noting a slight decrease in the value

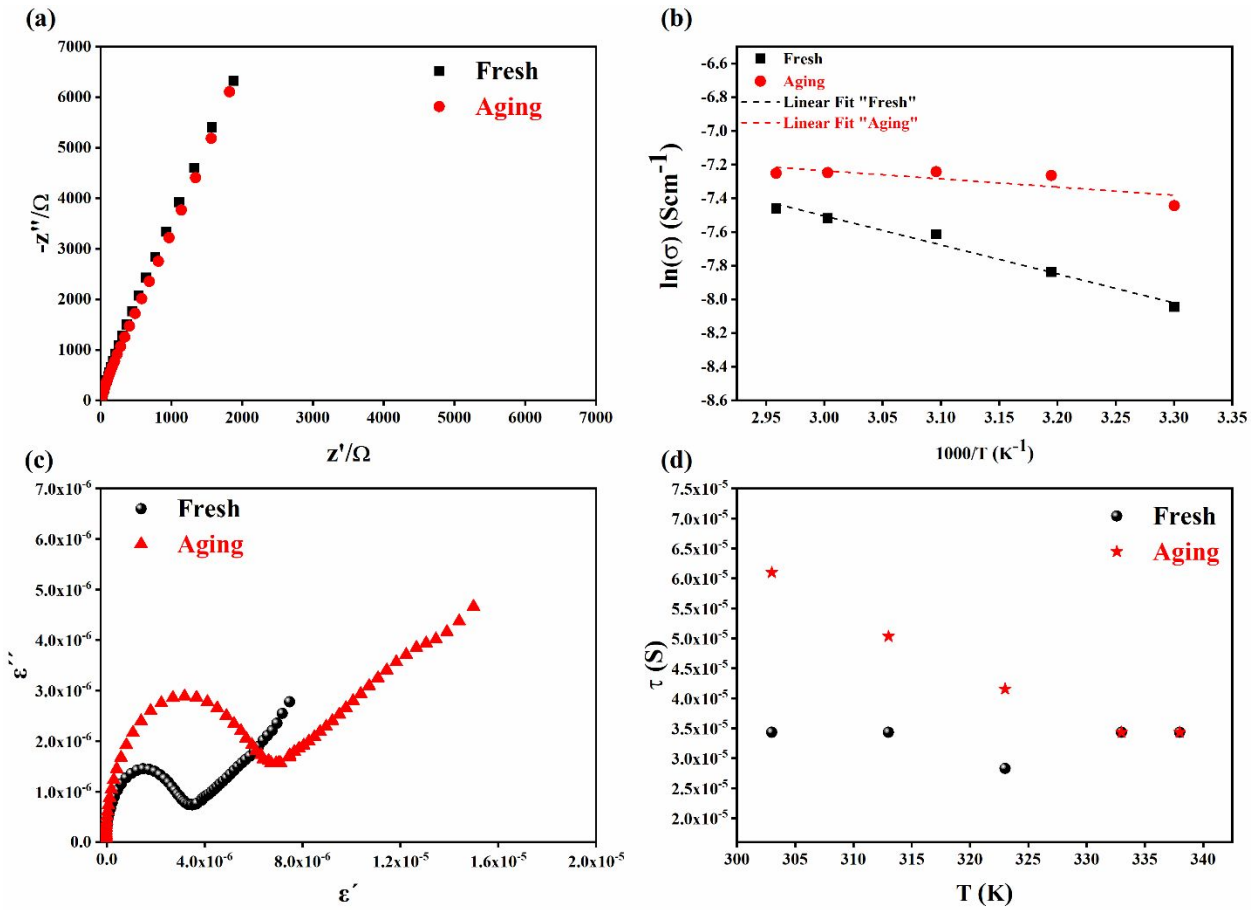

Fig. 3 a) Nyquist plots; (b) Arrhenius plot; (c) The Cole-Cole plot; (d) Relaxation time versus temperature; for fresh and aging HFE.

of the absorption edge from E_g~3.57 eV for fresh to E_g~3.49 eV for aging HFE. The high value of E_g reflect the dynamic structure of HFE and confirm the non-nucleophilic nature[18]. The extinction coefficient $K = \frac{\alpha\lambda}{4\pi}$ is an optical property reflects how the HFE species absorbs or reflects the electromagnetic radiation at a particular wavelength. **Fig. 2(e)** displays the k versus the wavelength (λ) of fresh and aging HFE, the value of k shows a significant decrease with increasing the wavelength in the UV period (200-340 nm) and is followed by a little increase with further increasing the wavelength. It can be noticed also that the value of k increases with increasing aging time. The refractive index (n) is an optical property of the sample that indicates

its ability to light bending; it can be calculated using the equation [19]: $n = \frac{(1+R)}{(1-R)} + \sqrt{\frac{4R}{(1-R)^2} - K^2}$, where $R = [1-(A+T)]$, A and T are the absorption and transmission coefficient respectively. Fig. 2f shows the profile of refractive index versus the wavelength (λ)of fresh and aging HFE, the behavior of n versus λ resembles the behavior of k versus λ. It can be noticed the evolution of new electronic absorption spectra at λ~ 483 and 643 nm with aging, which confirms changing the chemistry of the solvation species with storage. Based on the ATR-FTIR and UV-Visible findings, the average Mg^{2+} solvation shells in the HFE electrolytes are composed primarily of bound glyme and $(NO_3)^-_2$. Aging HFE results change the composition of the Mg^{2+} solvation shells to bound glyme, -C≡N−H-O(H)---Mg^{2+}, -C≡N---$Mg^{2+}$and $(NO_3)^-_2$. This behavior confirms the power of aging time on conditioning and speciation of HFE. **Fig. 3(a)** shows the Nyquist plot of the as-prepared fresh and aging electrolyte at 55 °C. The plot shows an incomplete semicircle at higher frequencies and a spike at low frequencies. The Zview software was applied to fit the semicircle curves and calculate the bulk resistance (the intersection value of the semicircle and the Z′ axis). The activation energy of the Mg^{2+} ions in the temperature range of 303-338 °C is determined by the Arrhenius equation: $\sigma = \sigma_o exp^{\frac{-E_a}{KT}}$, where σ_o, E_a and K represents the pre-exponential conductivity factor, the activation energy for ion conduction, and the Boltzmann constant. The lowest activation energy, ~ 0.042 eV (Table 1) is for aging HFE; its values are estimated from the linear fitting of the Ln (σ) vs. 1000/T plot, **Fig. 3(b).** This low value suggests the role of aging time in increasing the radius of solvation shells and reducing the ion-diffusion barrier hence optimizing the electrical parameters of the electrolyte. **Fig. 3(c)** shows the Cole-Cole plot of the real dielectric constant ε′ versus imaginary dielectric loss ε″ of the as-prepared fresh

Table 1 Electrical parameters of fresh and aging HFE.

Aging calendar	Conductivity at 303 K σ (S/cm)	Activation energy E_a(eV)	Transference number $t_{Mg^{2+}}$
Fresh	0.32×10^{-3}	0.148	0.74
Aging	0.59×10^{-3}	0.042	0.81

and aging electrolyte at 323K. The relaxation time τ was calculated from the maxima of the symmetric semicircle at $\tau\,\omega_{max} = 1$, where ω_{max} is the angular frequency of the maximum ε′′. The loss peak was observed to shift with the aging time and the temperature. This confirms the role of aging time in changing the viscosity of the HFE and the chemical environment of the Mg^{2+} charge carriers. **Fig. 3(d)** shows the variation of the relaxation time ln(τ) vs. 1000/T plot; the fresh electrolyte shows independence behavior while the aging electrolyte shows activation behavior with the temperature. **Fig. 4(a-b)** shows the Cole-Cole plot of Mg|Mg symmetric cells using fresh and aging HFE before and after DC polarization (ΔV=0.05V), the initial R_0 and steady-state R_s charge transfer resistances were calculated from the fitting of the semicircle curves. The Mg^{2+} ion transference numbers of fresh and aging HFE are calculated using Bruce and Vincent equation: $t_{Mg^{2+}} = \left[\frac{I_s(\Delta V - R_0 I_0)}{I_0(\Delta V - R_s I_s)}\right]$, [20] where I_0 and I_s refer to the initial current and the steady state current, respectively. It was observed that the value of $t_{Mg^{2+}}$ increases from ~ 0.74 to ~ 0.82 before and after aging,

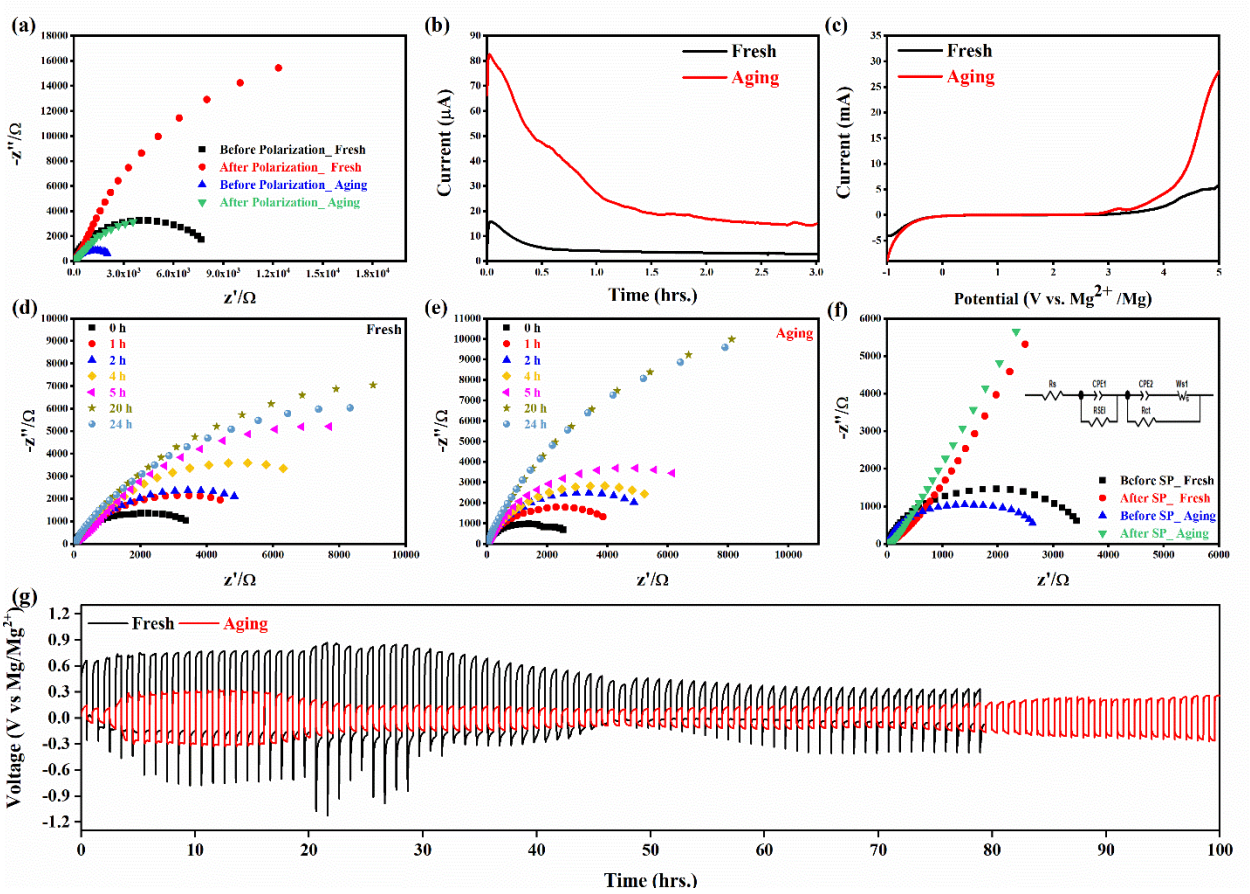

Fig. 4 (a) Nyquist plots of symmetric Mg|HFE|Mg cells before and after DC polarization; (b) Polarization current curve vs. time; (c) LSV curve of Mg|HFE|SS cells; Nyquist plots of symmetrical Mg|Mg cells (as a function of time) of (d) fresh (e) aging; (f) EIS spectra of Mg|HFE|Mg symmetric cells before and after Stripping/Plating(inset is the equivalent circuit); (g) Mg Stripping/Plating curves, of fresh and aging HFE.

respectively. This confirms the role of aging HFE in changing the chemistry of solvation species and the chemical environment surrounding the Mg^{2+} ions[21]. LSV was applied to demonstrate the electrochemical stability of the HFE electrolytes before and after aging; SS ||Mg cells are assembled using fresh and aging HFE. **Fig. 4(c)** shows the LSV curves covering an electrochemical window between -1 to 5 V with oxidation stability up 3 V before and after aging, however the aging HFE is more readily oxidized due to disruption of the ACN-Mg bonds that were grew up after aging as mentioned in ATR-FTIR section. **Fig. 4(d-e)** shows the EIS spectra of

Mg|Mg half cells at 25˚C using HFE before and after aging at different storage times. The spectra show a typical Nyquist plot with a depressed semicircle, the diameter of the semicircle increases with increasing storage time, and further the diameter is reduced with aging. This is due to the growth of the passivation layer at the anode/electrolyte interface and changing the solvation species due to aging, respectively. **Fig. 4(f)** displays the Nyquist plots of Mg|Mg half cells using fresh and aging HFE before and after stripping/plating. The inset figure is the equivalent circuit where the electronic element parameters were fitted using the ZView software. The values of the charge transfer resistance R_{ct} of Mg|Mg half cells using fresh and aging HFE before and after stripping/plating are 3454/2623 and 32610/28871 Ω, respectively. The drop in the value R_{ct} after aging confirms the role of aging calendar in reducing the Mg^{2+} solvation barrier as mentioned before, while the formation of anode electrolyte passive layer interface with cycling causing the aggravation of R_{ct}. **Fig. 4(g)** shows the time-dependent voltage curves vs. time of Mg|Mg half cells at 0.02 mA cm^{-2} (0.5h charge and 0.5h discharge) using fresh and aging HFE. The cell with aging HFE shows long-term cycling capability with low overpotential compared with fresh one; stripping/plating overpotential increased slightly with time and became stable after 20 cycles. Fig.5 shows SEM image and EDS map for Mg disc collected from Mg|Mg symmetric cells using fresh and aging HFE after stripping/plating for 20 cycles. The surface of Mg shows background with tightly packed morphology-based Mg and sticks morphology on the front based the residual Si from the fiber glass separator. The nature of the Mg electrolyte/electrode interface in fresh and aging HFE was studied using ATR-FTIR, **Fig. 5(d)** shows the ATR-FTIR spectra of bare Mg and Mg disc collected from Mg|HFE|Mg symmetric cells using fresh and aging HFE. It can be noticed that the intensity of the characteristic peaks of the Mg electrolyte/electrode interface

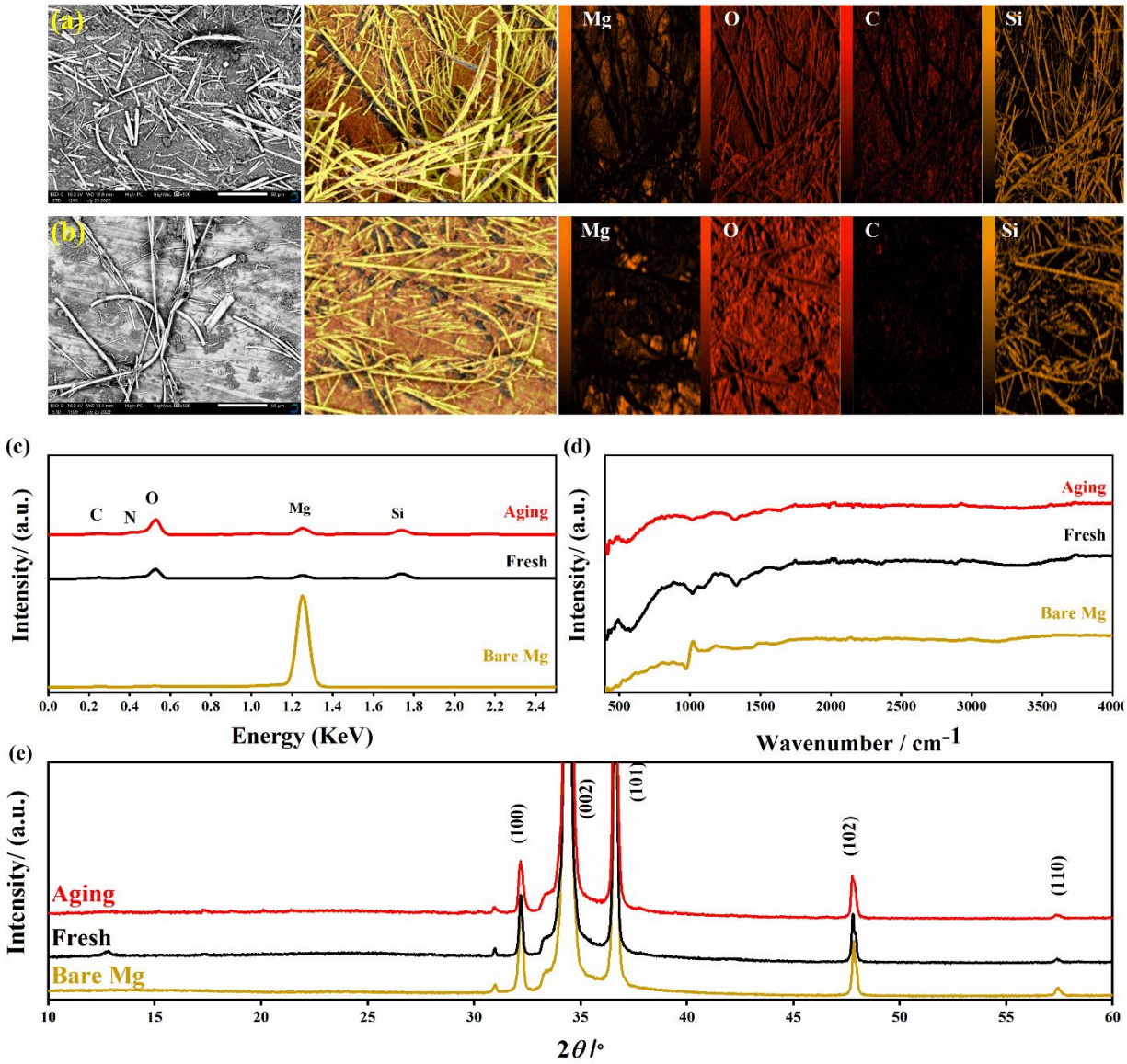

Fig. 5 SEM micrographs and corresponding mapping images of (a) Fresh and (b) aging; (c) EDX Spectra (d) ATR-FTIR Spectroscopy (e) XRD patterns of bare Mg, fresh, and aging HFE.

was reduced to low values after aging HFE, which confirms the role of aging time in tailoring the composition of the Mg^{2+} solvation shells to bound glyme, -C ≡ N−H-O(H)---Mg^{2+}, -C ≡ N---$Mg^{2+}$and $(NO_3)^-_2$ causing reduction in the solvation barrier of Mg^{2+} so does the crystallinity of the electrolyte/electrode interface compared with the fresh one. Fig. 5(e) illustrates the X-ray

diffraction (XRD) patterns of bare Mg and Mg disc collected from Mg|Mg symmetric cells using fresh and aging HFE; the pattern matches well with the lattice of hexagonal Mg (JCPDS No.901–3058)[18]. The reduction in the intensity values of the Bragg peaks coincides with the ATR-FTIR results and confirms a decrease in the crystallinity of the electrolyte/electrode interface. **Fig. 6a** shows the CV curves of Mg-S coin cell using fresh and aging HFE in a potential range of 0-2.6 V vs. Mg/Mg^{2+} with a scan rate of 20 mV s^{-1}. The cell with aging HFE shows relatively high anodic and cathodic current compared with the fresh HFE; further, the voltage interval of the redox peaks decreased, indicative of the role of aging on reducing the solvation barrier so it does enhance the electrochemical performance of the HFE. **Fig. 6(b)** shows the Nyquist plots of Mg-S cell using fresh and aging HFE, the EIS spectrum shows a depressed two semicircles response at the middle and high frequency regions and a long line in the low frequency region, representing the interphase contact resistance, the charge-transfer resistance and ion-diffusion process resistance, respectively.[22] EIS parameters were collected by simulating and fitting the experimental data using Randles electrical circuit-based model and ZView software (inset **Fig. 6b**). Where, R_s, R_{SEI}, R_{ct} and w_s are the Ohmic resistance of the bulk cell, the resistance of the interfacial layer, the charge-transfer resistance, and Warburg impedance, respectively. Table 2 displays the EIS electronic element parameters of Mg-S cell using fresh and aging HFE. It can be noticed that R_s, R_{SEI}, $R_{ct,}$ and w_s were reduced after aging, which confirms the role of aging in changing the Mg^{2+} solvation barrier of HFE species. The diffusion coefficient of magnesium ($D_{Mg^{2+}}$) was calculated by the equation: [22] $D_{Mg^{2+}} = \left[\frac{R^2T^2}{2A^2n^4F^4C^2\sigma^2}\right]$, the Warburg factor σ was calculated from the slope of the linear fitting $\omega^{-0.5}$ Vs Z' at low frequencies of the relation $Z' = R_s + R_{ct} + \sigma\omega^{-0.5}$, **Fig.6(c).**

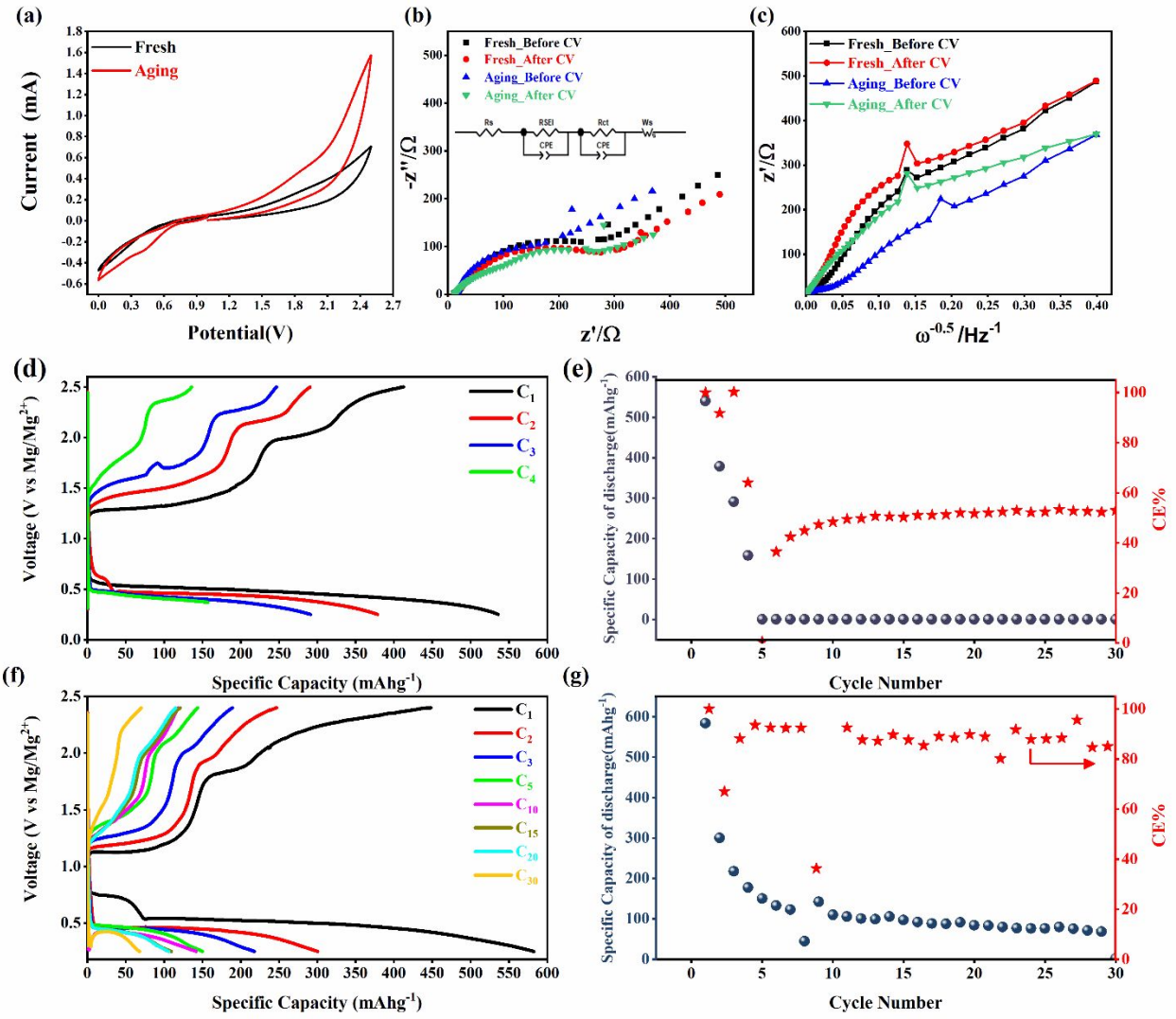

Fig. 6 (a) CV profiles (b) EIS spectra and inset is the equivalent circuit ; (c) $\omega^{-0.5}$ *Vs* Z' of Mg-S cells using fresh aging HFE; (d) Galvanostatic discharge-charge curves (e) Cycling performance and Coulombic efficiency versus cycle number of Mg|fresh HFE|S cell; (f) Galvanostatic discharge-charge curves; (g) Discharge capacity and Coulombic efficiency versus cycle number of Mg|aging HFE|S cell.

Table 2 Electrochemical impedance parameters of the fresh and aging HFE

EIS parameters	$R_s(\Omega)$	$R_{SEI}(\Omega)$	$R_{ct}(\Omega)$	CPE ($F\times10^{-4}$)	$\sigma(\Omega)$	$D_{Mg}{}^{2+}[cm^2.s^{-1}]$
Fresh	12.24	30.5	349.8	1.04	510.47	7.54×10^{-15}
Aging	10.96	25	323.4	2.23	466.74	9.01×10^{-15}

The σ values were ~ 510 and 466 Ω for the cell with fresh and aging HFE, respectively, indicating the aging electrolyte has relatively low Mg^{2+} diffusion barrier resulting in enhanced electrochemical performance of the aging HFE. The values of $D_{Mg^{2+}}$ of fresh and aging HFE are around 10^{-15} cm^2/s which is still low compared with the typical Mo_6S_8 ($\sim10^{-12}$ cm^2/s) intercalation cathode. **Fig. 6 d** and f display charge-discharge profiles of Mg-S coin cells with fresh and aging HFE at a current density of 0.02 mA cm^{-2}, respectively. The cell with aging HFE delivered a relatively higher initial discharge/charge capacity ~ 585/450 mAh g^{-1}. The discharge/charge curves exhibit two successive plateaus representing the conversion of higher-order polysulfides to lower-order polysulfides and vice versa, respectively. **Fig. 6 e** and g show the cycling stability profiles of Mg-S coin cells with fresh and aging HFE at a current density of 0.02 mA cm^{-2}, respectively. The cell with fresh HFE initially showed a high discharge capacity ~ 535 mAh g^{-1} but faded within four cycles to very low values, and the Coulombic efficiency dropped to < 60%. The cell with aging HFE initially showed a high discharge capacity of ~ 585 mAh g^{-1} but decreased within several cycles to ~100 mAh g^{-1} up to 30 cycles with Coulombic efficiency >90%. This can be attributed to the role of aging the electrolyte in altering the coordination interactions between the solvents and anions with Mg^{2+} so does the electrochemical stability. Furthermore, the short

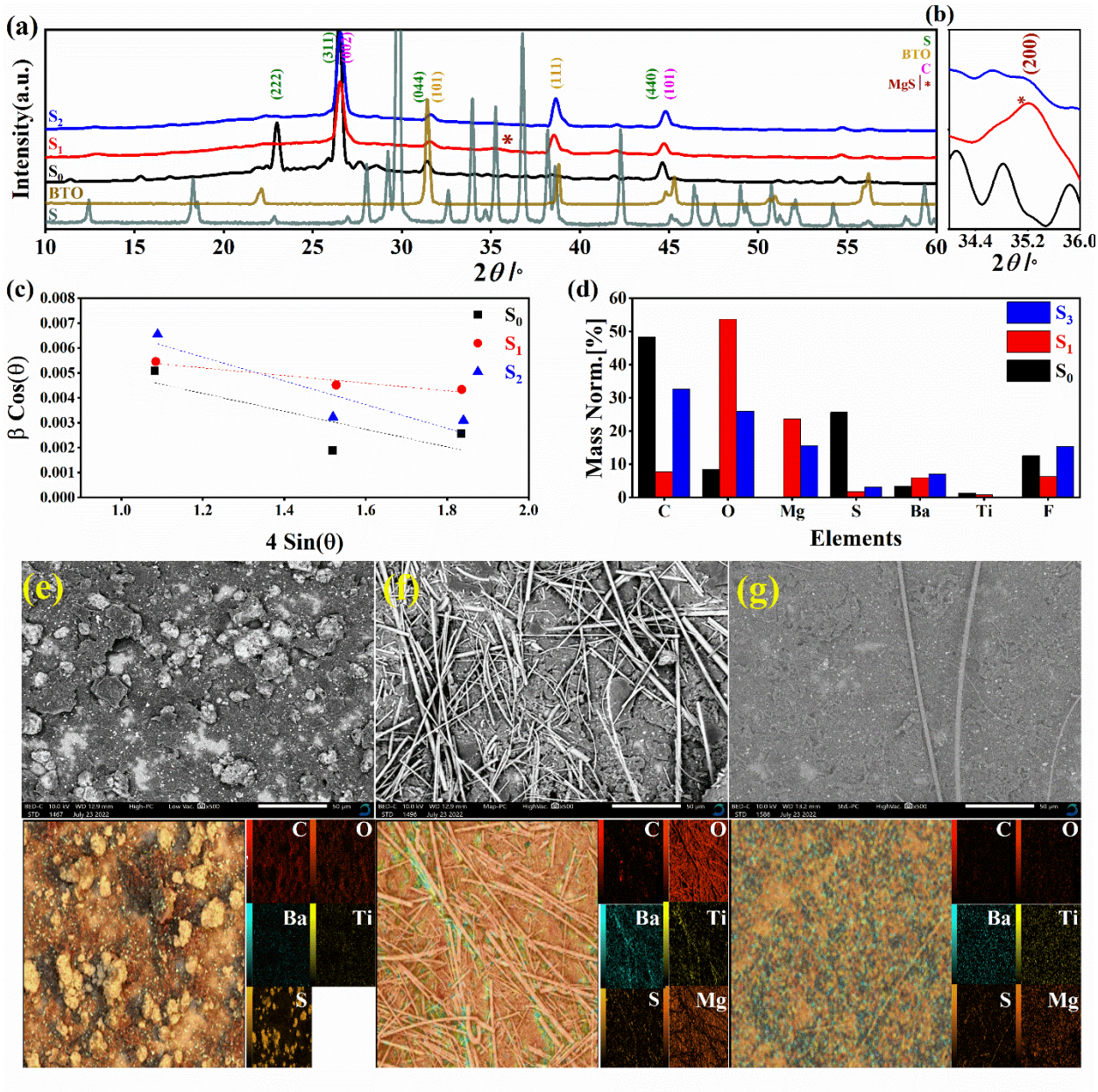

Fig. 7 (a) XRD pattern (b) Zoom in 2θ =34.0–36.0° (c) W-H analysis (d) EDS diagram of S_0, S_1 and S_2; SEM-mapping of (e) S_0, (f) S_1 and (g) S_2.

cycle life can be attributed to the formation of a discharge product with insulating nature like MgS as will be mentioned in the following XRD section. Future work will consider controlling the battery discharge to avoid oxidation process beyond the formation of MgS_2.[23] To further elucidate the mechanism of the conversion reaction, Mg-S coin cells with aging HFE were disassembled after initial discharge and discharge/charge. The S cathodes were collected and rinsed by ACN and dried at 80 °C for conducting further characterization. **Fig. 7(a)** shows the XRD patterns of the S cathode in the pristine state (S0), after discharge (S1), and after recharge (S2). This pattern helps us to trace the interplay between the structure evolution of the S cathode with varying its electrochemical states (pristine→discharge→charge). The pattern of the pristine electrode S_0 shows a set of Bragg diffraction peaks at 23°, 25.74°, 28.58°, 31.37°, and 34.83° match the (222), (026), (313), (044), and (333) reflection planes which represent the diffraction peaks of the orthorhombic S (DB Card No.: 9011362, Fddd:2). After discharge (S1), the main diffraction peak (222) shows intensive broadening, and the other characteristic peaks show a noticeable reduction. After recharging, the broadness of the main diffraction peak (222) still exists, and the other peaks partially restored the original intensity. **Fig. 7(b)** shows the zoomed-in 2θ=34.5° of MgS corresponding to the (200) plane; that peak did not exist in the pristine state it grew up after discharge and reduced after recharge[24]. All these results confirm the disrupted structure skeleton of S due to the insertion of Mg^{2+} via conversion reaction from S_8 to short and long-chain magnesium polysulfide. The work extended to study the structural deformation of the S cathode using the sensitivity of the diffraction pattern to the crystallite size and lattice strain upon insertion/extraction of Mg^{2+}. Williamson-Hall equation[25]: $\beta\, cos\theta = \frac{k\lambda}{D} + 4\varepsilon\, sin\theta$,where β is full width at half maximum (FWHM), θ is the Bragg's angle, k is the shape factor (0.94) and λ is the X-ray wavelength, was applied to examine strain of the S cathode with varying its electrochemical

states. **Fig. 7(c)** shows Williamson-Hall diagram: βcos(θ) versus 4sin(θ) of S_0, S_1 and S_2, the slope of the line and the y-intercept represent the strain and crystallite

Table 3 Lattice parameters of the cathode using Bragg law and UDM (W-H plot) at different electrochemical states; S_0, S_1 and S_2.

Sample	Strain (ε) $\times 10^{-3}$	Crystallite Size $D(nm)$
S_0	3.59	17.06
S_1	1.53	20.54
S_2	4.77	12.75

size, respectively[26]. Table 3 lists the lattice parameters of the S cathode-based materials using Bragg law and UDM (W-H plot) at different electrochemical states; S_0, S_1, and S_2. It can be noticed that the value of the strain decreases from 3.59 (S0) to 1.53 (S1) upon discharge (Mg^{2+} insertion) and re-increases upon charge (S2);(Mg^{2+}= extraction), which confirms the Mg^{2+} insertion/extraction in the framework of the S cathode is accompanied by structure deformation caused by volume expansion/contraction[27]. **Fig. 7(d)** shows EDS analysis of S_0, S_1, and S_2; the results display the content of Mg increase from 0 in the pristine state (S_0) to 23.68 wt.% in the discharge state (S_1) and decreases to 15.6 wt.% after recharge (S_2). EDS data coincide well with XRD data, confirming the conversion reaction between magnesium ions and sulfur atoms. **Fig. 7e** shows SEM-EDS mapping for S_0 with uniform deposition of S particles on the surface of the carbon flakes, which confirms that the microwave-assisted cathode preparation method is a powerful tool for designing promising sulfur-based cathodes[28]. After discharge (S_1), the SEM-EDS mapping shows a homogeneous distribution of Mg and S in the background and micro-stick

surface morphology in the front of the image, Fig. 7(e). After the charge, the image displays smooth surface morphology with a homogeneous distribution of Mg and S.

Conclusion

In this work, we have demonstrated the aging time calendar of the HFE as a conditioning step to achieve low overpotential and reversible Mg electrodeposition and stripping. Spectroscopic analyses reported changes in the Mg^{2+} solvation shells of aging HFE to bound glyme, -C≡N−H-O(H)---Mg^{2+}, -C≡N---$Mg^{2+}$and $(NO_3)^-_2$ compared with bound glyme and $(NO_3)^-_2$ for the fresh one. Mg-S cells using aging HFE delivered an initial discharge capacity of ~ 585 mAh g^{-1}. Still, it decreased within several cycles to ~100 mAh g^{-1} up to 30 cycles with Coulombic efficiency >90% compared with the Mg-S cell with fresh HFE which initially showed a high discharge capacity but faded within four cycles. The Coulombic efficiency dropped to < 60%. Ex-situ XRD, SEM, and EDS-Map of the S cathode at different electrochemical states confirmed the reversible conversion reaction $Mg+S_8 \leftrightarrow MgS_n$ accompanied by structural deformation of the S skeleton caused by volume expansion/contraction due to insertion/extraction of Mg^{2+}. The aging electrolyte calendar offers a new approach to optimize a kind of Mg electrolyte, and the design concepts can potentially develop efficient electrolytes for magnesium battery applications.

Acknowledgments

This work is financially supported by the Academy of Scientific Research Technology/ Bibliotheca Alexandrina (ASRT/BA) (Grant No. 1530) and the Science Technology Development Fund (Grant No. 30340) from Egypt. Professor N. S. would like to thank the financial support

from the National Science Foundation NSF CAREER Award (grant no. 2047753) and NSF MRI for the acquisition of the advanced FESEM (grant no. 1919919). Proposal Development Grant from the University of Massachusetts Boston is acknowledged.

References

(1) Li, X.; Liu, Q.; Wang, X.; Liu, J.; Cheng, M.; Hu, J.; Wei, T.; Li, W.; Ling, Y.; Chen, B. A facile in situ Mg surface chemistry strategy for conditioning-free Mg [AlCl4] 2 electrolytes. *Electrochimica Acta* **2022**, *414*, 140213.

(2) See, K. A.; Liu, Y.-M.; Ha, Y.; Barile, C. J.; Gewirth, A. A. Effect of concentration on the electrochemistry and speciation of the magnesium aluminum chloride complex electrolyte solution. *ACS applied materials & interfaces* **2017**, *9* (41), 35729-35739.

(3) Zhao-Karger, Z.; Liu, R.; Dai, W.; Li, Z.; Diemant, T.; Vinayan, B.; Bonatto Minella, C.; Yu, X.; Manthiram, A.; Behm, R. J. r. Toward highly reversible magnesium–sulfur batteries with efficient and practical Mg [B (hfip) 4] 2 electrolyte. *ACS Energy Letters* **2018**, *3* (8), 2005-2013.

(4) Sheha, E.; Farrag, M.; Fan, S.; Kamar, E.; Sa, N. A Simple Cl–-Free Electrolyte Based on Magnesium Nitrate for Magnesium–Sulfur Battery Applications. *ACS Applied Energy Materials* **2022**, *5* (2), 2260-2269.

(5) Li, Y.; Zuo, P.; Zhang, N.; Yin, X.; Li, R.; He, M.; Huo, H.; Ma, Y.; Du, C.; Gao, Y. Improving electrochemical performance of rechargeable magnesium batteries with conditioning-free Mg-Cl complex electrolyte. *Chemical Engineering Journal* **2021**, *403*, 126398.

(6) Hou, S.; Ji, X.; Gaskell, K.; Wang, P.-f.; Wang, L.; Xu, J.; Sun, R.; Borodin, O.; Wang, C. Solvation sheath reorganization enables divalent metal batteries with fast interfacial charge transfer kinetics. *Science* **2021**, *374* (6564), 172-178.

(7) Sun, Y.; Wang, Y.; Jiang, L.; Dong, D.; Wang, W.; Fan, J.; Lu, Y.-C. Non-nucleophilic electrolyte with non-fluorinated hybrid solvents for long-life magnesium metal batteries. *Energy & Environmental Science* **2023**.

(8) Zhou, Y.; Lu, X.; Zheludkevich, M.; Wang, F. Tailoring corrosion and discharge performance of Mg anode by corrosion inhibitor. *Electrochimica Acta* **2022**, *436*, 141471.

(9) Dlugatch, B.; Mohankumar, M.; Attias, R.; Krishna, B. M.; Elias, Y.; Gofer, Y.; Zitoun, D.; Aurbach, D. Evaluation of Mg [B (HFIP) 4] 2-based electrolyte solutions for rechargeable Mg batteries. *ACS Applied Materials & Interfaces* **2021**, *13* (46), 54894-54905.

(10) Attias, R.; Salama, M.; Hirsch, B.; Goffer, Y.; Aurbach, D. Anode-electrolyte interfaces in secondary magnesium batteries. *Joule* **2019**, *3* (1), 27-52.

(11) Barile, C. J.; Barile, E. C.; Zavadil, K. R.; Nuzzo, R. G.; Gewirth, A. A. Electrolytic conditioning of a magnesium aluminum chloride complex for reversible magnesium deposition. *The Journal of Physical Chemistry C* **2014**, *118* (48), 27623-27630.

(12) Gao, H.; Ning, S.; Zou, J.; Men, S.; Zhou, Y.; Wang, X.; Kang, X. The electrocatalytic activity of BaTiO3 nanoparticles towards polysulfides enables high-performance lithium–sulfur batteries. *Journal of Energy Chemistry* **2020**, *48*, 208-216.

(13) Yacout, N.; Refai, H. S.; Kebede, M. A.; Salman, F.; Sheha, E. Significant study of BaTiO3 as a cathode for magnesium battery applications. *Materials Chemistry and Physics* **2022**, *292*, 126770. DOI: https://doi.org/10.1016/j.matchemphys.2022.126770.
(14) Farrag, M.; Refai, H.; Sheha, E. The role of adding NaF to the electrolyte in constructing a stable anode/electrolyte interphase for magnesium battery applications. *Journal of Solid State Electrochemistry* **2023**, *27* (2), 379-389.
(15) Reimers, J. R.; Hall, L. E. The solvation of acetonitrile. *Journal of the American Chemical Society* **1999**, *121* (15), 3730-3744.
(16) Dereka, B.; Lewis, N. H.; Keim, J. H.; Snyder, S. A.; Tokmakoff, A. Characterization of acetonitrile isotopologues as vibrational probes of electrolytes. *The Journal of Physical Chemistry B* **2021**, *126* (1), 278-291.
(17) Chen, X.; Kuroda, D. G. Ionic Conduction Mechanism in High Concentration Lithium Ion Electrolytes. *Chemical Communications* **2023**.
(18) Farrag, M.; Refai, H.; Sheha, E. The role of adding NaF to the electrolyte in constructing a stable anode/electrolyte interphase for magnesium battery applications. *Journal of Solid State Electrochemistry* **2022**, 1-11.
(19) Muhammad, F. F.; Aziz, S. B.; Hussein, S. A. Effect of the dopant salt on the optical parameters of PVA: NaNO3 solid polymer electrolyte. *Journal of Materials Science: Materials in Electronics* **2015**, *26* (1), 521-529. Rajesh, K.; Menon, C. Estimation of the refractive index and dielectric constants of magnesium phthalocyanine thin films from its optical studies. *Materials letters* **2002**, *53* (4-5), 329-332.
(20) Zugmann, S.; Fleischmann, M.; Amereller, M.; Gschwind, R. M.; Wiemhöfer, H. D.; Gores, H. J. Measurement of transference numbers for lithium ion electrolytes via four different methods, a comparative study. *Electrochimica Acta* **2011**, *56* (11), 3926-3933.
(21) Diederichsen, K. M.; McShane, E. J.; McCloskey, B. D. Promising routes to a high Li+ transference number electrolyte for lithium ion batteries. *ACS Energy Letters* **2017**, *2* (11), 2563-2575.
(22) Liu, Y.; Wang, Y.; Wang, H.; Dou, S.; Tian, H.; Gan, W.; Yuan, Q. Dynamic template directed construction of three-dimensional porous bismuth aerogels for high-rate Na-ion storage. *Journal of Materials Chemistry A* **2023**, *11* (11), 5945-5955.
(23) Vincent, S.; Chang, J. H.; Canepa, P.; García-Lastra, J. M. Mechanisms of Electronic and Ionic Transport during Mg Intercalation in Mg–S Cathode Materials and Their Decomposition Products. *Chemistry of Materials* **2023**.
(24) Zhang, R.; Cui, C.; Xiao, R.; Li, R.; Mu, T.; Huo, H.; Ma, Y.; Yin, G.; Zuo, P. Interface regulation of Mg anode and redox couple conversion in cathode by copper for high-performance Mg-S battery. *Chemical Engineering Journal* **2023**, *451*, 138663.
(25) Chauhan, A.; Verma, R.; Kumari, S.; Sharma, A.; Shandilya, P.; Li, X.; Batoo, K. M.; Imran, A.; Kulshrestha, S.; Kumar, R. Photocatalytic dye degradation and antimicrobial activities of Pure and Ag-doped ZnO using Cannabis sativa leaf extract. *Scientific reports* **2020**, *10* (1), 1-16.
(26) Javadian, S.; Zeinodiny, A.; Dalir, N.; Gharibi, H.; Ghavam, S. J. Facile one step self-template synthesis of NixMgMn2O4 (X= 0.12 to 0.50) alloys as a promising cathode for magnesium ion battery. *Materials Chemistry and Physics* **2023**, *298*, 127447.
(27) Papandrea, B.; Xu, X.; Xu, Y.; Chen, C.-Y.; Lin, Z.; Wang, G.; Luo, Y.; Liu, M.; Huang, Y.; Mai, L. Three-dimensional graphene framework with ultra-high sulfur content for a robust lithium–sulfur battery. *Nano research* **2016**, *9*, 240-248.
(28) Sheha, E. M.; Farrag, M.; Refai, H.; El-Desoky, M.; Abdel-Hady, E. Positron Annihilation Spectroscopy as a Diagnostic Tool for Probing the First ‐ Cycle Defect Evolution in Magnesium ‐ Sulfur Batteries Electrodes. *physica status solidi (a)*.